# Strain-gradient crystal plasticity model with slip-system level GND tracking: simulation vs experiment for sequential strain path change in AA6016-T4

Rishabh Sharma[a], Russell Marki[b], Asher Webb[a], Marko Knezevic[b],
Michael P. Miles[c], David T. Fullwood[a]

[a]Department of Mechanical Engineering, Brigham Young University, Utah, USA

[b]Department of Mechanical Engineering, University of New Hampshire, New Hampshire, USA

[c]Manufacturing Engineering Department, Brigham Young University, Utah, USA

## Abstract

Crystal plasticity models that track strain gradients and associated geometrically necessary dislocations (GNDs) typically determine the Nye tensor, mimicking the experimental approach. However, estimating GND densities for each slip-system is then intrinsically ambiguous. This study seeks to build upon current state of the art by quantifying GNDs at the slip-system level in the model using the local strain gradients. The model is exercised by replicating experiments undertaken on AA6016, which are performed under multi-step strain paths; both GND and SSD populations are quantified at various stages using both high resolution EBSD (HREBSD) and XRD. A full 3D volume of the material is extracted using ion beam serial sectioning to enable the creation of a high-fidelity model of the material.

The combined modeling and experimental campaigns conclude that: 1) Calculation of the GND content at the slip level gives effectively equivalent GND evolution as the tradition Nye tensor method, but provides the significant advantage of knowing unambiguously the contribution on each slip system. 2) The net hardening predicted by the SGCP model is accurate, including prediction of a rapid increase in hardening (and associated dislocation content) following strain path change; and 3) Comparisons of observed and simulated GND populations reveal that buildup in the real sample is dominated by precipitate distribution rather than by grain boundary (GB) networks; such precipitates are not present in the current model, hence this result was not predicted.

## 1. Introduction

Hardening behavior during deformation of metals is generally strongly tied to dislocation evolution. Early crystal plasticity (CP) models typically applied a phenomenological hardening law, with no explicit dislocation quantification, but with isotropic hardening on a given slip system being tied to the amount of slip that had occurred [1]. In order to account for observed nuances is hardening behavior, evolution of dislocation populations began to be explicitly tracked by the models, with dislocations further being categorized as forest or parallel dislocations, for example [2]. The resistance to applied loads can be thought of as a local friction stress associated with statistically stored dislocations (SSDs). However, such models do not account for kinematic hardening, which plays a vital role during unloading, reverse loading and other strain path changes, such as those experienced during automotive panel forming operations. Backstresses experienced during such complex loading are generally associated with the long-range stress fields arising from geometrically necessary dislocations (GNDs).

Nye, Kroner and others have shown how GNDs can be quantified from a knowledge of the plastic strain gradients about a given point [3, 4]. Since strain fields are locally mapped by many CP finite element codes, it is a relatively straightforward task to quantify GND content [2, 5, 6]. At one level of implementation these dislocations simply contribute to the overall friction type flow stress [2]; a more complex implementation associates a backstress to the local GND populations in the form of a microforce [6]. Generally the Nye tensor is determined using the curl of the plastic strain field, and then densities on different slip systems can be estimated from an under-constrained set of equations, leading to a non-unique mapping onto the individual systems [7, 8].

This paper builds upon previous work with advances in both the modelling strategy, and in terms of the experimental data obtained for guiding and validating the model. A Gurtin type strain gradient CP (SGCP) model is implemented (based upon the theory presented in [9]), but with the GND density calculated directly at the slip system level from the slip gradients; i.e. the full Nye tensor, with resultant ambiguity in slip-level GND content, is not calculated. Backstress development is not incorporated into this version of the model. It is confirmed that the calculated GND content from the new approach is consistent with the Nye tensor approach. Furthermore, both the GND content and the SSD content are experimentally determined at various points of a 2-stage deformation in AA6016 sheet using high resolution EBSD (HREBSD) and XRD. Multi-strain path forming is undertaken by pre-straining aluminum alloy (AA) 6016-T4 samples under biaxial tension followed by subsequent in-situ uniaxial tension. The experimental dataset captures total dislocation and GND density, texture, sub-grain plastic strain, and macroscopic stress-strain response at key points in the multi-strain deformations. A full 3D volume was constructed via serial sectioning to characterize the GND distribution at various depths and the grain structure of the final deformed material for accurate implementation of the model. Correlations between GND distributions and microstructural features (such as grain size, precipitates and GBs) are analyzed, along with the net Burgers vector fields for both the experimental and simulated material response.

The evolution of GNDs is discussed in many previous paper, including theory development by Ashby [10] and experimental observations by Shen et al. [11]. Ashby explains the evolution of GNDs near GB to maintain the strain accommodation due to differing deformation modes of the neighboring grains. Shen observes GND pileups at the GB due to Frank-Reed sources and peculiarities of the microstructure, such as slip incompatibility across the GB. However, various studies have noted that in order to fully explain, and accurately predict, sub-grain strain and strain

gradients, it is insufficient to observe 2D characteristics and behavior from a surface scan of the microstructure [12, 13] but the full 3D structure is required. A statistical volume element (SVE) is needed that embodies the actual grain morphology and local texture in order for the SG-CPFE model to have a hope of capturing the correct local deformation response. Several open-source data analysis packages, such as Dream.3D, offer the capability of generating synthetic SVEs. Synthetic SVEs tools generally generate 3D elements with grain orientation, shape and size statistics that match the information from a 2D experimental map. Apart from the fact that the 2D information may not be representative of the 3D morphology, important descriptors such as small grains and edges, which influence the strain gradient development, are often neglected in the simulated SVEs. As described by Hall and Petch, grain size plays a significant role in the deformation response of polycrystalline metal alloys [14, 15]. The importance of grain size effects on strain gradient crystal plasticity analysis is further echoed by several authors [16-18]. Hence, the current study presents an effective and high-fidelity replacement of simulated SVEs with a measured SVE for accurate modeling of multi-strain path forming. Combined EBSD and serial sectioning via broad ion beam milling provides a relatively inexpensive approach to high-volume data collection compared with synchrotron radiation measurements (for example).

## 2. Experimental procedure

The metal for this study was provided by Commonwealth Rolled Products. Aluminum 6016 alloy was processed and received in T4 aged condition. The composition of the AA6016-T4 is given in Table 1. The experiments in this study were guided by a previous study on AA6016-T4 by Sharma et al. [19] (see that paper for illustrations of the Marciniak tooling setup and sheet dimension). The virgin material had a grain size (determined by EBSD, describe later) of 32 μm, 30 μm, and 18 μm, when measured on the surfaces perpendicular to the rolling, transverse and

normal directions, respectively. The sheet specimens were aligned along the rolling direction (RD) and ASTM-E8 uniaxial tension specimens were pulled at a 1.5 mm/min crosshead displacement rate and the force-strain data was recorded using a load cell and extensometer. Specimens of as-received sheet material were tested uniaxially to fracture for the calibration of hardening parameters of the modeling campaign. Square specimens were deformed under biaxial tension using an Interlaken Hydraulic press. The blanks were restrained using small lock beads in the clamping system. Standard Marciniak tooling was employed, with a 100 mm diameter flat-topped punch. A carrier blank between the sheet specimen and the punch was introduced to distribute strain and avoid pre-mature localization. A total clamp load of 200 kN was applied and friction between all the surfaces in contact (between the punch, carrier blank, and sheet specimen) was minimized by a combination of mineral oil and 0.5 mm thick Teflon sheets. The normal direction (ND) surface of the sheet specimens was patterned using a polymer-based black paint, speckled over a layer of white paint, to measure surface strains. 2-D strain maps were obtained by employing the DIC approach, using the Aramis system from Trillion Quality Systems [20]. The captured series of deformation images were processed through Aramis software to produce surface strain maps and ensure uniform biaxial deformation.

*Table 1 Nominal chemical composition of AA6016-T4*

| Sample | Al | Si | Mg | Fe | Mn | Zn | Cu | Ti | Cr |
|---|---|---|---|---|---|---|---|---|---|
| AA6016 | 96.4-98.8 | 1.0-1.5 | 0.25-0.6 | 0-0.5 | 0-0.2 | 0-0.2 | 0-0.2 | 0-0.15 | 0-0.1 |

After pre-straining under biaxial tension, scaled-down ASTM-E8 tensile samples (gauge length 15.8 mm, total length, with reduced length grips, of 31.6 mm) were extracted from the central uniform-strain region of the sheet for subsequent in-situ uniaxial tension straining. These are termed ‘pre-strained specimens’ in the current study. Waterjet-cut pre-strained specimens were

temporarily mounted (using polymeric bond) on the flat surface of round 9-inch diameter aluminum pucks for metallographic sample processing. The ND surface of specimens was first ground with grits of 400, 600, 800, 1200, and 1200 fine abrasive paper. The glue was then dissolved in acetone to prepare the ground surface for electron-backscattered diffraction (EBSD) data collection by electropolishing in an electrolyte solution of 1:9 ratio of perchloric acid and methanol under 20 volts and 2 amps at room temperature for 30 seconds. The final result was a slightly etched surface. While severe etching can result in a surface topography that negatively affects EBSD results, the etch was mild, and the HREBSD results from the surface were consistent with HREBSD performed at sub-surface layers that were exposed via ion beam serial sectioning.

Polished pre-strained specimens were subjected to subsequent uniaxial straining using an in-situ stage. The surface strains were recorded by employing HRDIC. We note that for the purposes of this paper, the HRDIC is being used merely as a digital extensometer; the value of the HRDIC will be more apparent in future comparisons with model predictions. Strains were tracked of an initial 250x250 sq. μm region that was marked using a micro-indenter (Fig. 1a). A speckle pattern was applied by loosely depositing copper particles onto the polished ND surface, following a similar method to that pioneered by Carroll et al. [21] (few details are included in the published paper, but were shared with the authors directly by Carroll), and using the same design of in-situ stage. For depositing the pattern, the powder was passed through a series of filter paper layers with a 10 μm pore size using compressed air to capture most of the big powder particles and avoid concentration of the powder in clumps. A final pattern with a random distribution of particles ranging from 0.3-0.2 μm was obtained (Fig. 1b). High-resolution scanning electron microscope (SEM) images were captured at approximately every 1.2% strain. The captured images were processed through GOM Aramis software (Fig. 1c).

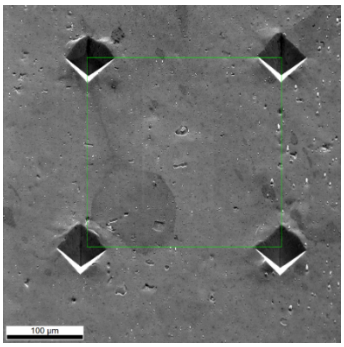


*Micro-indents*

(a)

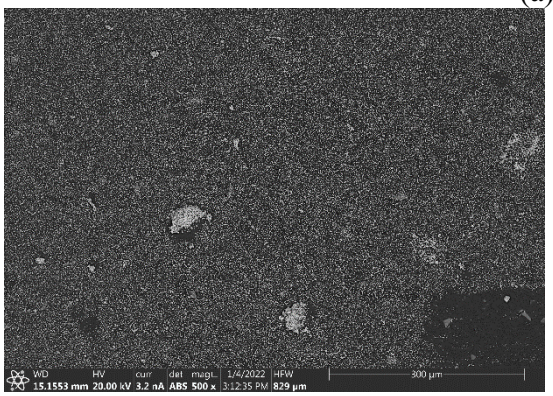


*SEM image of the DIC pattern*

(b)

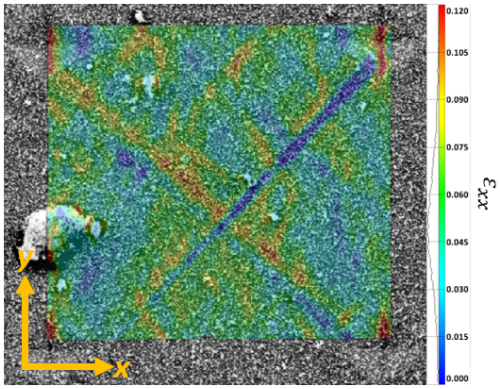


*Surface strain map*

(c)

*Figure 1 HRDIC process to measure surface strains under in-situ uniaxial tension: a) the region of interest marked by micro-indents, b) image of the copper powder pattern around the ROI, c) a map of strain in the x-direction from the HRDIC software*

After recording the surface strains via HRDIC, the deposited Cu powder pattern was cleaned in an ultrasonic cleaner, first using acetone (for 10 mins), then methanol (for 10 mins) and finally using ethanol (for 5 mins). As illustrated in Fig. 2, the sample was then subjected to serial sectioning for 3D data collection, in an inert Argon gas environment of a JEOL ion-beam cross-section polisher. The surface of the sample was milled at an angle of 85° from the horizontal (a glancing angle of 5°) to produce a close-to-even surface finish (Fig. 2a). The broad ion beam has a diameter of 3000 µm which covered the entire region of interest (ROI) well. The surface was first coarsely milled at 5 kV and 4.2 atm for 20 mins which removed most of the material. A second

finer step removed unevenness by milling the surface at 4 kV and 6.2 atm for 10 mins. The milled layer depth was calculated by measuring the profile of the indents using Zeta instruments' 3D optical profilometer (Fig. 2b). A line scan from the 3D optical measurement was then extracted to plot and analyze the vertical depth of the indents. Minor aberrations in the measurements were manually corrected by fitting a trend on the general profile of the indent to accurately project the vertical depth (Fig. 2c). The process was repeated for all four indents in the ROI to measure an average of 2.56 µm milled layer after each (combined coarse and fine) milling step.

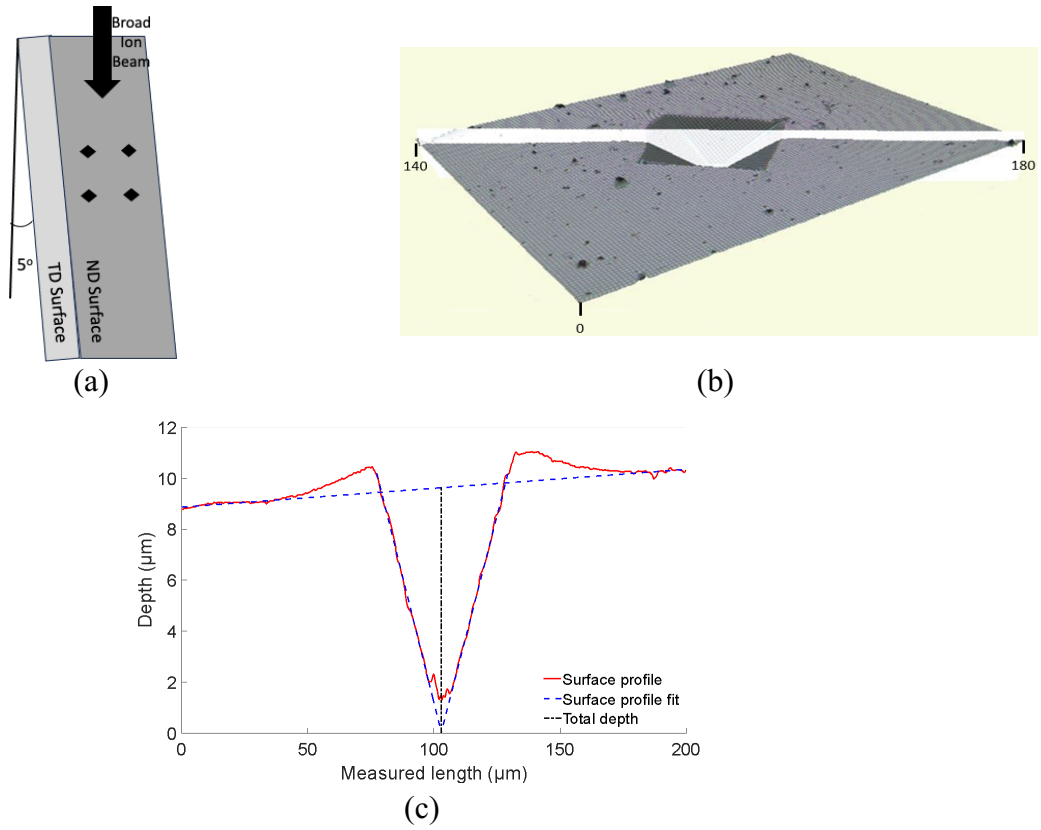


*Figure 2 Schematic depicting serial sectioning and milled layer measurements*

The sample was milled up to a total depth of 87.04 µm and sequential EBSD data was collected from a 300x300 sq. µm region after each milling step. The polished surfaces of the samples were analyzed using EDAX OIM software (2010) to index the aluminum (FCC) phase. A 20 keV beam with an accelerating voltage and a spot size of 3.2 nano-amps was utilized, along

with a dwell time of 100 nanoseconds. The exposure was set to 8.10, with a gain of 500 and a step size of 1 μm for the EBSD camera. Additionally, 2x2 binning was employed for the Kikuchi patterns to achieve a maximum frame rate of 115 $s^{-1}$, thus optimizing the scan time.

The layers at 0 μm, ~21.76 μm, ~43.52 μm, ~65.28 μm, and ~87.04 μm of the SVE were processed for GND analysis and scanned using slightly different EBSD parameters. For these scans, 1x1 binning was used to obtain high-quality Kikuchi patterns, allowing for post-scan High-Resolution EBSD (HREBSD) processing with a maximum frame rate of 75 $s^{-1}$. The collected EBSD data was first processed through EDAX OIM software to crop out the indents and surrounding deformation regions. These regions were eliminated from all subsequent analyses because of modifications in the original microstructure due to strains induced in the sample surface by the indents. A 190x190 sq. μm layer along with accurate milled depth measurement was fed to the open-source Dream.3D software to create a stack of layers. A user-specified Dream.3D pipeline with a series of post-processing filters was used to create a 3D SVE of the EBSD-scanned layers. The pipeline yielded a final SVE volume of dimensions 150x150x87.04 μm (Fig. 3). It is noted that the SVE is extracted from a deformed sample, and therefore does not accurately represent the undeformed material. However, a single average orientation is assumed within each grain of the modeled SVE, removing the strain gradients resulting from deformation, while not necessarily correcting for texture evolution and grain fragmentation during deformation. Producing an SVE via non-destructive methods for a sample of the size required for these experiments is difficult, and not available to the authors; the method followed seems to be a reasonable compromise.

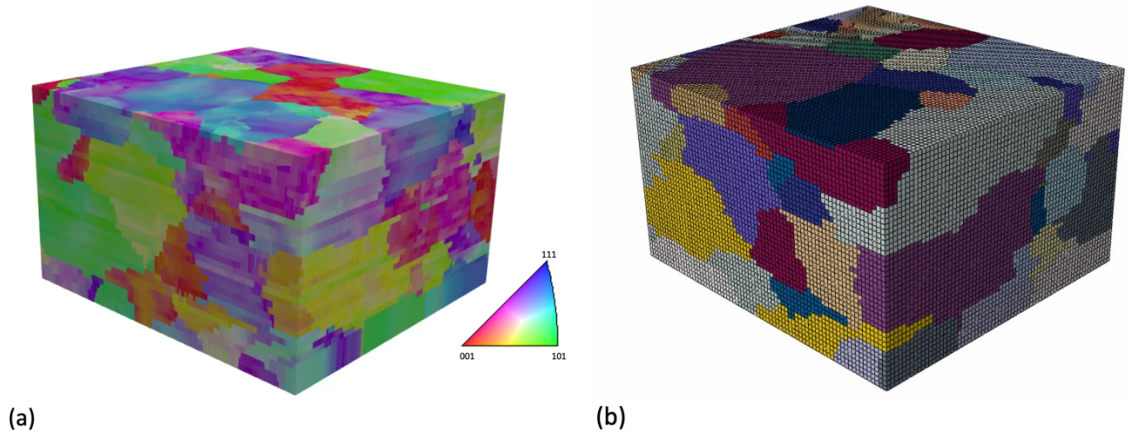


*Figure 3 EBSD scan and Dream.3D SVE output (a) & mesh as inputted to ABAQUS (b). The dimensions for both figures are 150x150x87.04 µm.*

During EBSD data collection, Kikuchi patterns were saved at various stages of forming (unstrained → pre-strain → post subsequent in-situ strain) to map GND density. In this study, the HR-EBSD technique was employed to calculate the GND density using OpenXY. Three different areas of 90x90 sq. µm with 3 µm step size, from each sample (unstrained, pre-strained, and subsequent strained) were used to plot GND. The GND calculations are based on the dislocation density tensor ($\boldsymbol{\alpha}$) introduced by Nye:

$$\rho \approx \frac{1}{b}\|\boldsymbol{\alpha}\|_1 \, , \boldsymbol{\alpha} = \nabla \times \boldsymbol{\beta} \tag{1}$$

where ρ is dislocation density, b is the Burgers vector size, $\boldsymbol{\beta}$ is the elastic distortion as measured by HREBSD, and $\|\boldsymbol{\alpha}\|_1$ is the $L_1$ norm on a tensor (the sum of the absolute values of its components). Total dislocation density was measured using x-ray analysis. The measured diffracted x-ray peaks were processed through convolutional multiple whole profile (CMWP) fitting open-source software developed at Eötvös Loránd University by Dr. Tamás Ungár and collaborators [22, 23]. CMWP calculates total dislocation density (DD) by measuring the peak broadening effect which indicates irregularities in a lattice. Other methods are available, such as the method of moments [24], but it relies on the same physics; the results from both methods for

total dislocation density have been seen to be in agreement. The measured total DD of 5.46e13 (from CMWP) and GND density of 4.83e13 (from HREBSD) for the virgin material indicates that the statistically stored DD of 6.3e12 is reasonable. These values were used as input parameters to the SG-CPFE model.

Precipitates were identified semiautomatically from EBSD maps. Contiguous regions of low confidence index (as identified by the EBSD software) were assumed to be indicative of the presence of a precipitate. Backscatter electron (BSE) images taken in the same region as the EBSD maps were then used to confirm precipitate presence as indicated by regions of white in the maps (Fig. 4). Pixels associated with precipitates are removed from the GND calculations by OpenXY, and shown on the GND map as having zero GND (dark blue on the color scale). By comparing the GND map (the right images in Fig. 4) with the BSE image on the left, one can see that precipitates are correctly identified by this method. Note that the identification of precipitates is subject to the EBSD map resolution; only precipitates that are bigger than the step size of 1 μm are identified.

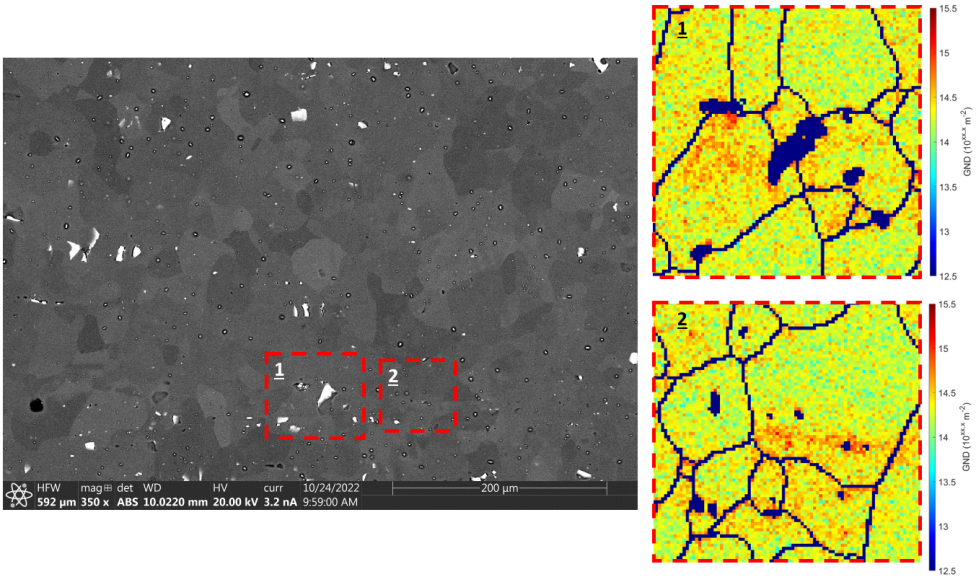


*Figure 4 Backscattered electron (BSE) micrograph (left) and corresponding HREBSD GND maps (right) of certain section for unstrained AA6016-T4 sheet*

## 3. SG-CPFE

A single crystal elasto-viscoplastic crystal plasticity model is employed as a constitutive law within the FEM to relate a pair of work-conjugated stress and strain measures at every integration point of finite elements [1]. The formulation is briefly summarized below for completeness and to appreciate the new strain gradient formulation. The total deformation gradient tensor given by Abaqus, $\mathbf{F}$, at each integration point is multiplicatively decomposed into an elastic stretching and lattice rotation part, $\mathbf{F}^*$, and the plastic part, $\mathbf{F}^p$, embedding the crystallographic slip deformation

$$\mathbf{F} = \mathbf{F}^*\mathbf{F}^p \tag{2}$$

The stress-strain relations are

$$\mathbf{T}^* = \mathbf{C}\mathbf{E}^* \tag{3}$$

$$\mathbf{T}^* = \mathbf{F}^{*-1}\{(det\mathbf{F}^*)\boldsymbol{\sigma}\}\mathbf{F}^{*-T} \tag{4}$$

$$\mathbf{E}^* = \frac{1}{2}\{\mathbf{F}^{*T}\mathbf{F}^* - \mathbf{I}\} \tag{5}$$

where $\mathbf{C}$ is the fourth rank elastic stiffness tensor based on crystal orientation and $C_{11} = 108.2$ GPa, $C_{12} = 61.3$ GPa, and $C_{44} = 28.5$ GPa,, $\mathbf{T}^*$ is the second Piola–Kirchhoff stress, $\mathbf{E}^*$ is the Green-Lagrangian strain tensors, and $\boldsymbol{\sigma}$ is the Cauchy stress. The flow rule for $\mathbf{F}^p$ is

$$\dot{\mathbf{F}}^p = \mathbf{L}^p\mathbf{F}^p \tag{6}$$

$$\mathbf{L}^p = \sum_s \dot{\gamma}^s \mathbf{b}_o^s \otimes \mathbf{n}_o^s \tag{7}$$

where $\dot{\gamma}^s$ is the shearing rate on a given slip system $s$, while $\mathbf{b}_o^s$, and $\mathbf{n}_o^s$ denote the slip system direction and slip plane normal, respectively, in the total Lagrangian framework denoted by the subscript '$o$'. The power-law is used for the shearing rate [25-27].

$$\dot{\gamma}^s = \dot{\gamma}_0^s \left(\frac{|\tau^s|}{\tau_c^s}\right)^{\frac{1}{m}} sign(\tau^s) \tag{8}$$

where, $\tau^s$ is the resolved shear stress driving force ($\tau^s = \mathbf{T}^* \cdot \mathbf{b}_o^s \otimes \mathbf{n}_o^s$) on the slip system $s$, $\tau_c^s$ is the resistance to slip, which will be described shortly, $\dot{\gamma}_0^s$ is a reference slip rate of 0.001 $s^{-1}$, and

m is the strain rate sensitivity constant of 0.05. To complete the theory incorporating the texture evolution, the crystal lattice spin, $\mathbf{W}^*$, is

$$\mathbf{W}^* = \mathbf{W}^{app} - \mathbf{W}^p \tag{9}$$

$$\mathbf{W}^p = \frac{1}{2}(\mathbf{L}^p - \mathbf{L}^{pT}) \tag{10}$$

where $\mathbf{W}^{app}$ is the applied spin over the polycrystal and $\mathbf{W}^p$ is the plastic spin. The numerical implementation of the above theory is described in detail in [1].

The constitutive model summarized above implements a hardening law based on the evolution of statistically stored dislocation density (SSD) for the evolution of slip resistance [28, 29]. This approach builds upon the work originally presented in [30]. The model is advanced here to include GNDs. The densities of dislocations evolved originally solely based on a thermally activated rate law with shearing on slip systems [31]. The slip resistance, $\tau_c^s$ , for $\{111\}\langle 110\rangle$ slip systems *s* is calculated. The $\tau_c$ is the sum of three contributions as follows [27, 32-35]

$$\tau_c^s = \tau_0 + \tau_{DD}^s + \tau_{sub} \tag{11}$$

Where $\tau_0$ is a friction stress fitted to predict yield stress, and embeds the Peierls stress, barrier effect due to grain size, and any content of initial dislocation density (SSD and GND). The term does not evolve with plastic strain. The remaining two terms contribute to the evolution of slip resistance owing to the build up of dislocation density (SSD and GND) and substructure/debris, $\tau_{DD}^s$ and $\tau_{sub}$, respectively. These two terms evolve according to the Taylor-type relations [36-38].

$$\tau_{DD}^s = \chi b\mu \sqrt{\sum_{s\prime} L^{ss\prime}\,(\rho_{SSD}^{s\prime} + \rho_{GND}^{s\prime})} \tag{12}$$

$$\tau_{sub} = 0.086\mu b\sqrt{\rho_{sub}}\,log\left(\frac{1}{b\sqrt{\rho_{sub}}}\right) \tag{13}$$

where simulated $\sum_s \rho_{GND}^s$ will be compared against HREBSD measurements from the experiments, $\rho_{sub}$ is the substructure/debris dislocation density, which evolves from a very small magnitude 0.1, $b$ is

the Burgers vector, $\mu$ is the shear modulus $(26\,GPa)$, $\chi$ is a dislocation interaction factor [39] taken to be 0.7, and $L^{ss'}$ is the latent hardening matrix [40].

The initial density of the unstrained SSD is set to 6.3e12/12 and GND to 4.83e13/12 per slip system, *s*, consistent with the measurements on virgin material. SSD evolves based on the balance between the rate of generation and the rate of removal of dislocations i.e. dynamic recovery [38, 41, 42],

$$\frac{\partial \rho_{SSD}^{s}}{\partial \gamma^{s}} = \frac{\partial \rho_{gen,SSD}^{s}}{\partial \gamma^{s}} - \frac{\partial \rho_{rem,SSD}^{s}}{\partial \gamma^{s}} = k_1\sqrt{\rho_{SSD}^{s}} - k_2(\dot{\varepsilon},T)\rho_{SSD}^{s} \tag{14}$$

with $k_1$ as a fitting coefficient for statistical trapping and $k_2$ as a rate-sensitive coefficient defined by

$$\frac{k_2}{k_1} = \frac{\chi b}{g}\left(1 - \frac{kT}{Db^3} ln\,(\frac{\dot{\varepsilon}}{\dot{\varepsilon}_o})\right) \tag{15}$$

In Eq. (3.15), $k$, $\dot{\varepsilon}_o$, $g$, and $D$ are a Boltzmann constant, a reference strain rate of $10^7$ $s^{-1}$, an activation enthalpy, and drag stress, respectively. The last two constants are also fitting constants. Finally, the rate of debris DD evolves using

$$\Delta\rho_{sub} = qb\sqrt{\rho_{sub}}k_2\sum_{s}\rho_{SSD}^{s}|\Delta\gamma^{s}| \tag{16}$$

with $q$ as a rate fitting coefficient. The coefficient determines a fraction of dislocations that lead to debris formation, while the rest is assumed annihilated.

While the above-described dislocation density based crystal plasticity model can be regarded as a standard formulation, the current model has been advanced to enable the calculation of GNDs through a strain gradient formulation. Thus, while most of the models in the literature take the curl of plastic distortion or deformation gradient directly [9], our formulation takes gradients of slip rates. As such, there is significant novelty in the current approach, as the computation of slip rate gradients enables the model to quantify GNDs per slip system. In the

CPFE model, the displacement gradient is additively decomposed into elastic and plastic contributions as: $\mathbf{H} = \mathbf{H}^e + \mathbf{H}^p$, where $\mathbf{H}^p$ is defined as the sum of shears ($\gamma^s$) over all active slip systems, and $\mathbf{H}^p = \sum_s \gamma^s \mathbf{b}^s \otimes \mathbf{n}^s$. As shown by Nye [43], the density of GND dislocations can be quantified by a second rank tensor, which is defined as the curl of the plastic distortion ($\text{curl}\ \mathbf{H}^p$) as [44] $\mathbf{G} = \nabla \times \mathbf{H}^p = \sum_s (\nabla \gamma^s \times \mathbf{b}^s) \otimes \mathbf{n}^s = b \sum_s \left( \rho_{\vdash}^s \mathbf{t}^s \otimes \mathbf{b}^s + \rho_{\odot}^s \mathbf{b}^s \otimes \mathbf{b}^s \right)$, where $\mathbf{t}^s = \mathbf{n}^s \times \mathbf{b}^s$. The quantities $\tilde{\rho}_{\vdash}^s$ and $\tilde{\rho}_{\odot}^s$ are the weighted GND densities (directional derivatives of slip) and are defined as: $\rho_{\vdash}^s = -\frac{1}{b} \nabla \gamma^s \cdot \mathbf{b}^s$, $\rho_{\odot}^s = \frac{1}{b} \nabla \gamma^s \cdot \mathbf{t}^s$, where $\vdash$ and $\odot$ represent the edge and screw components of the GND densities, respectively. The total GND density on slip system, *s*, is defined as the magnitude: $\rho_{GND}^s = \sqrt{(\rho_{\vdash}^s)^2 + \left(\rho_{\odot}^s\right)^2}$.

The total GND density on a slip system thus requires a calculation of $\nabla \gamma^s$. This vector is computed through the non-local values of $\gamma^s$ at selected integration points at and around a given material point. The values of $\gamma^s$ are used in the quadratic interpolation function. An equivalent to the quadratic interpolation function is a linear version as

$$\begin{bmatrix} 1,\ x_1,\ y_1,\ z_1,\ x_1y_1,\ z_1y_1,\ z_1x_1,\ x_1y_1z_1 \\ 1,\ x_2,\ y_2,\ z_2,\ x_2y_2,\ z_2y_2,\ z_2x_2,\ x_2y_2z_2 \\ \cdots \\ 1, x_n,\ y_n,\ z_n,\ x_ny_n,\ z_ny_n,\ z_nx_n,\ x_ny_nz_n \end{bmatrix}_{nx8} \begin{bmatrix} c_1^s \\ c_2^s \\ \cdots \\ c_i^s \end{bmatrix}_{8x1} = \begin{bmatrix} \gamma_1^s \\ \gamma_2^s \\ \cdots \\ \gamma_n^s \end{bmatrix} \tag{17}$$

where there are $n$ integration points and $i$ terms in the polynomial used to approximate the spatial distribution of $\gamma^s$. While we show the linear interpolation in Eq. (3.17) for simplicity, we used the quadratic interpolation over 40 integration points to evaluate $\nabla \gamma^s$ at a given point embedded in between the 40 points. The coefficients $c_i$ can then be used to define a $\gamma^s(x, y, z)$ interpolation function of which the gradient can be readily taken. Given $\nabla \gamma^s$, $\rho_{GND}^s$ is evaluated and used in the hardening law.

## 4. Results and discussion

Figure 5 shows the hardening curve under uniaxial tension for specimens cut along the RD and TD directions. As can be seen, there is only a modest difference in behavior. Synthetic grain structures from Dream.3d were populated with orientations consistent with the texture measured from the virgin material (see [45] for the texture), and model hardening parameters were fit (Table 2 and Table 3) to the experimental RD data, and then the TD curve was predicted. Table 3 contains the latent hardening parameters that define $L^{ss\prime}$, the latent hardening matrix in Eq. 12 [40] which is also known as the dislocation interaction matrix that defines the potential interactions of dislocations with each other; $a_0$ is for self-interactions, $a_1$ for coplanar interactions, $a_2$ for colinear interactions, $a_3$ for glissile junctions, $a_4$ for Hirth junctions, and $a_5$ for Lomer Lock junctions. The model correctly predicts the slight lowering in yield stress and subsequent hardening behavior.

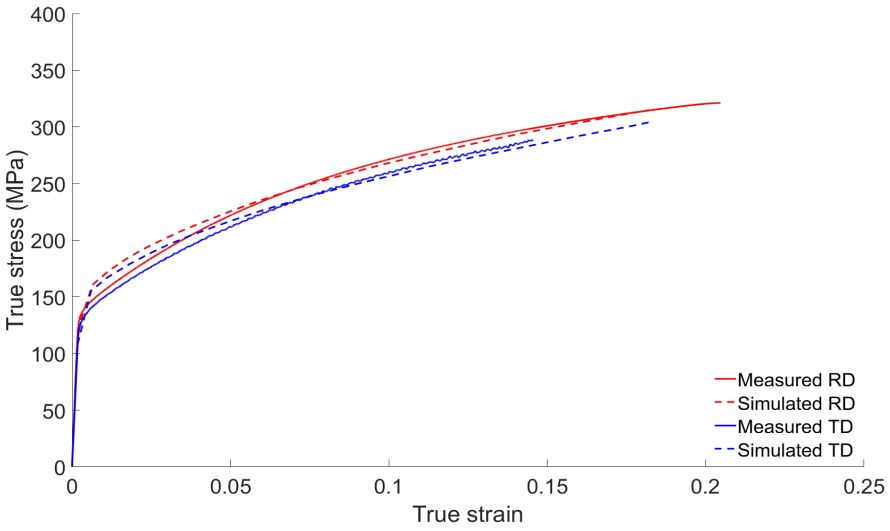


*Figure 5 Uniaxial tension work hardening curves of AA 6016 T4 specimens*

*Table 2 Hardening parameters*

| $\tau_0$ [MPa] | g | D [MPa] | $k_1$ | q |
|---|---|---|---|---|
| 40 | 0.1 | 60 | 1.08e7 | 2 |

*Table 3 Latent hardening parameters established in [46, 47] for FCC metals*

| a0 | a1 | a2 | a3 | a4 | a5 |
|---|---|---|---|---|---|
| 0.068 | 0.068 | 0.0454 | 0.625 | 0.137 | 0.122 |

The dislocation evolution (both GND from HREBSD and total density from XRD) due to work-hardening for biaxially pre-strained specimens, and subsequent uniaxial tension, are shown in Fig. 6. The overall dislocation density of the material is a combination of SSDs and GNDs. SSDs generally accumulate due to dislocation-dislocation interactions and mutual trapping in the crystal lattice, while GNDs accumulate in the strain gradient fields required to satisfy the geometric constraint of the crystal lattice arrangement. The total DD follows an evolution given by $\sim\varepsilon^{0.6}$ up to failure. In comparison, the growth in GND density is much slower, with trends that are almost flat in comparison to total DD. The consequence of these trends is that GNDs account for a higher

percentage of the total DD early in the deformation, while the fraction of SSDs becomes significantly larger at high strain which is apparent upon taking a ratio of GND and DD for biaxial tension pre-strain, in agreement with Ashby's observation (Ashby, 1970).

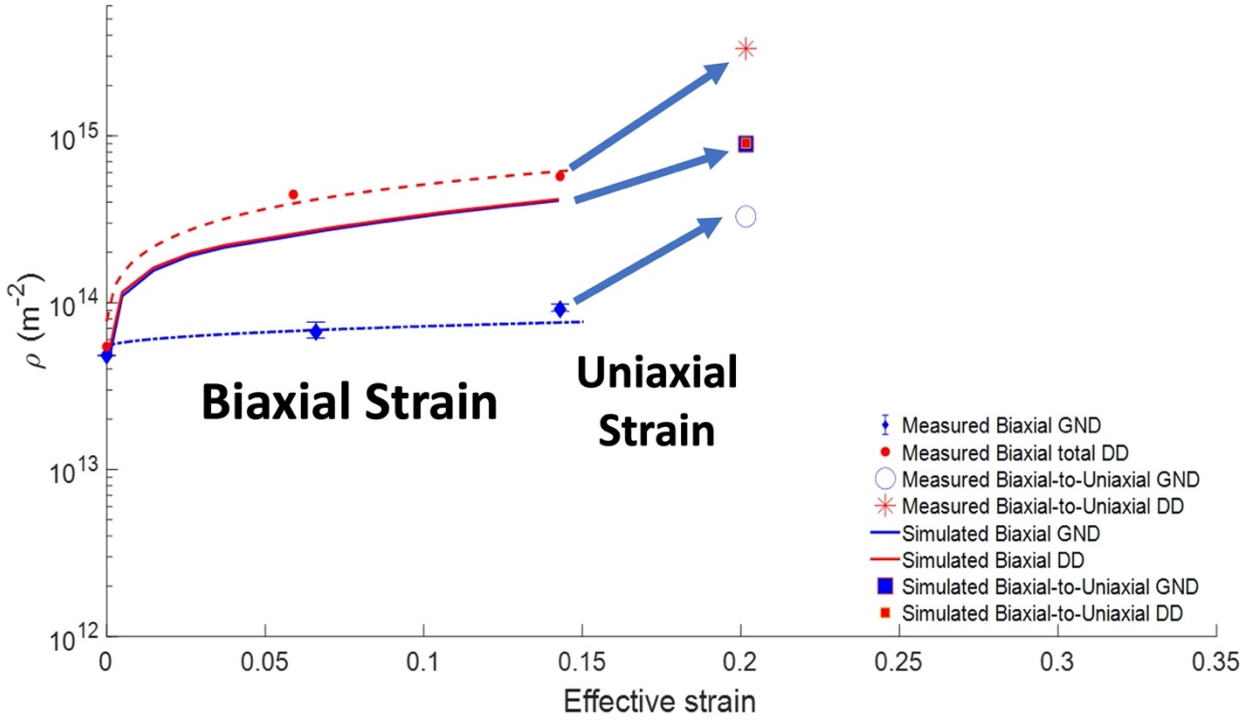


*Figure 6 GND development (blue lines and markers) and total dislocation density (red lines and markers). Dashed lines are measured values (HREBSD for GND and XRD for total dislocation density (DD)), and solid lines are simulated values. The final markers to the right of the curves are data for samples pre-strained to ~15% pre-strain, and then pulled a further 5.9% under uniaxial tension.*

The asterisk and open circle in Fig. 6 represent DD and GND densities (respectively) for samples pulled under biaxial tension to approximately 15% strain, followed by 5.9% deformation in uniaxial tension (which was pre-fracture). While the rates of both DD and GND density accumulation are fairly steady with strain during biaxial deformation, a change in strain path results in a much more rapid accumulation of both DD and GND density. One might assume that the higher dislocation density following strain path change might lead to faster exhaustion of ductility; however, the biaxial-to-uniaxial strain path reached 5% higher strain-to-failure than pure uniaxial deformation (not shown on the figure). When combined with the significantly lower yield

stresses observed after strain path changes (yield stress after 15% biaxial effective pre-strain is ~250 MPa, compared with ~300 MPa following the same amount of uniaxial pre-strain; Fig. 10 in [19]), it appears that latent hardening on non-active systems during biaxial deformation is significantly lower than self-hardening on the active slip systems. When the strain path changes, flow stress on the newly activated systems is significantly lower than on the originally active systems, and self-hardening on the newly active systems occurs rapidly, leading to a rapid increase in DD. It is interesting that GND density also increases rapidly due to the strain path change (i.e., as well as DD), indicating a similar increase in strain gradients to accommodate potential strain incompatibility on the new systems. In fact, motivation for incorporating strain gradients / backstress in the SG-CPFE model relates to changes in yield stress and other stress-strain characteristics following strain path changes, as discussed in a previous study of the same material [19].

Also shown in Fig. 6 are the dislocation density values simulated by the SG-CPFE model. Measured values were input as the initial values for the model, and the hardening parameters for the model were calibrated using a single uniaxial tension test. From the figure it is clear that the model predicts the shape of the total dislocation curve extremely well, with only a relatively small underprediction. However, the contribution of GNDs to the total density is much higher in the model than for the measured values, indicating that some tuning is required in the modeling parameters. While CPFE models have tunable latent hardening and self-hardening parameters, these are generally calibrated against the relatively small information contained in a uniaxial-tension stress-strain curve (potentially including texture information, although latent hardening has been found to have a small effect on texture evolution) [48]. The insights from this study indicate the potential need for more detailed validation of the model SG-CPFE model, including

not only several stress-strain curves relating to different strain paths, but also tuning of both DD and GND accumulation rates.

In order to check that the new approach to calculating GND density at the slip system level gave equivalent GND content to the more traditional Nye tensor approach, a simulated volume of the material containing twelve grains was modeled using both approaches. The sample was deformed in uniaxial tension, and the overall GND content was calculated via both methods. Figure 7 demonstrates that both methods predict almost equal overall GND content. Generally, there are only small differences (<5%) manifest at the grain level, apart from almost 60% difference between the two approaches for grain 9 at the highest level of strain. The evolution of GNDs is integrated into the DD hardening model via Eq. (12). The Nye tensor obtained from the gradient of slip rates and the Nye tensor obtained from the widely used curl of the plastic distortion or deformation gradient (curl $\mathbf{F}^p$) are nearly identical. An advantage of taking the gradient of slip rates is that it allows for the direct calculation of GND density per slip system, whereas using the curl of the plastic distortion yields the sum of GNDs over the slip systems. The sum is then distributed across slip systems according to their relative activity levels at every integration point using $\rho_{GND}^{s} = \rho_{GND}^{sum} \frac{\dot{\gamma}^{s}}{\sum_{s\prime} \dot{\gamma}^{s\prime}}$. Both methodologies result in similar overall (sum over the slip systems) GND density (Figure 7).

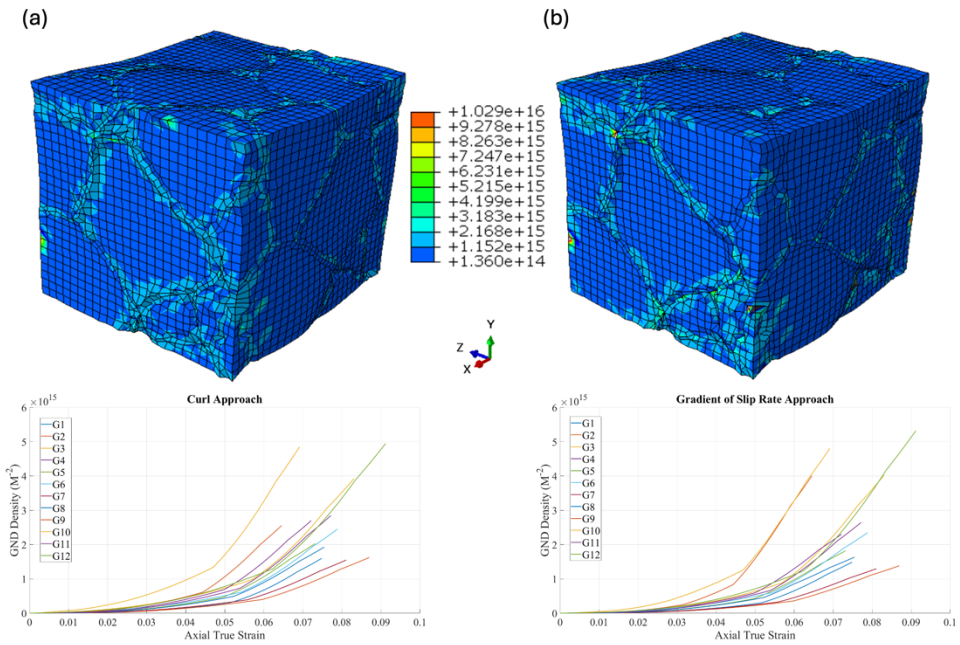


*Figure 7 Comparison of GND fields predicted for a 12 grains FE sample, based on (a) $curl(\boldsymbol{F}^p)$ and (b) $\nabla\gamma^s$, after tension is applied along the x-direction to an overall strain of 0.1. At the bottom of each figure are average GND density per grain vs plastic strain for the 12 grains in each model.*

Figure 8 shows the relationship between grain size and GND density in the biaxial-to-uniaxial sample. The relationship between the two microstructure variables is weak – the p value is 2.25%, indicating a statistically significant relationship, but the $R^2$ value is only 0.14. However, it is interesting to note that the relationship is positive. Usually one would expect that smaller grains have a higher GB area-to-volume ratio, resulting in high GND content, due to strain gradients near GBs. This was observed in a recent large survey of grains in a Ta polycrystal [49]; the statistical relationship was also weak, but the trend was significantly negative - i.e. larger grains generally had lower average GND content. This is an important point for the more detailed discussion of GND distribution below.

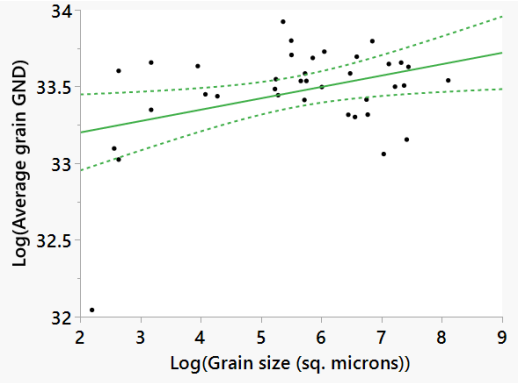


*Figure 8 Correlation between grain size and average grain GND density*

2 point statistics were employed to map the statistical geometrical relationships between GBs and GNDs, with an approach similar to that take by Ruggles et al. in a study relating GND content to specific phases in steel [50]. To determine an average geometrical relationship between GND content and GBs at individual scanned pixels, the position of GB pixels was assigned a value of 1, and other pixels were assigned a value of 0 in the image $I_{GB}$. The resultant image was then convolved with the map of GNDs (captured in the map, $I_{GND}$), as shown in the following equation:

$$f_2^{GB,GND} = \mathcal{F}^{-1}[(\mathcal{F}(I_{GB}))^* \cdot \mathcal{F}(I_{GND})]/N_{GB} \tag{18}$$

In the above equation, $\mathcal{F}$ represents the Fourier transform, and $()^*$ represents the complex conjugate of a term; $N_{GB}$ is the number of points in the GB network. A similar approach is taken for precipitates in the EBSD map. A precipitate was taken to be a connected region of 6 pixels or more with a confidence index below 0.1, and which was not already identified as belonging to the GB network. This identification process is justified further below by comparing SEM images with EBSD maps.

Maps of the 2-point statistics from the experimental measurements are shown in Fig. 9a,b; note that the GND values for both the plots is on a log scale. An example area showing the GND buildup at individual precipitates is shown in Fig. 10, and discussed below. The origins of the plots

in Fig. 9 denote the representative positions of GBs or precipitates; the value of GND density close to the origin indicates the average GND concentration near to GBs or precipitates, depending upon the map. In these maps taken from experimental data, the central point takes a value of zero because GND values are set to zero along the GB lines and within precipitates. The statistics for points near to the origin are also lowered based upon the size and shape of regions with zero GND density. From the map for precipitates (Fig. 9b), where the regions of zero GND are larger than those for GBs, this region is relatively small and does not affect the interpretation made below, as long as it is acknowledged. Taking into account this small region about the origin, the GND density is nevertheless reduced in the vicinity of GBs, while increasing around precipitates. There is ~21% higher average GND density within 10 μm of precipitates (Fig. 9b) compared to the density near GBs (Fig. 9a); there is a ~14.6% decrease in the GND density around the GBs compared to the average GND density. Sperry et al. observed strong strain gradients at all GBs in FCC Ni-superalloy, along with local orientation gradients associated with increased GND density [51]. Similarly, Hansen et al. observed significant GND accumulation at GBs and triple junctions in BCC Ta [49]. Hence, the lack of accumulation of GNDs at GBs in the Al sheet deformed in this study is an unexpected finding but helps to explain the surprising positive correlation between grain size and GND content (Fig. 8); i.e., this relates to the fact that GBs are not a primary cause of GND accumulation.

Figure 9 also compares the 2-pt. statistics trends in the GND development around the GBs as measured and as predicted for ~21.76 milled depth layer in a biaxially pre-strained specimen subjected to 5.86% subsequent uniaxial strain. Figure 9c applies the identical 2-point analysis to GNDs and GBs in the simulated deformed sample for comparison with the experimental data shown in Fig. 9a; note that there are no precipitates explicitly assumed in the simulation for

comparison with Fig. 9b. The simulation incorrectly predicts a strong correlation between GNDs and GBs. Such a correlation would typically be expected in many materials (as discussed above). The results demonstrate that precipitates would need to be added to the model to better capture trends in GND evolution.

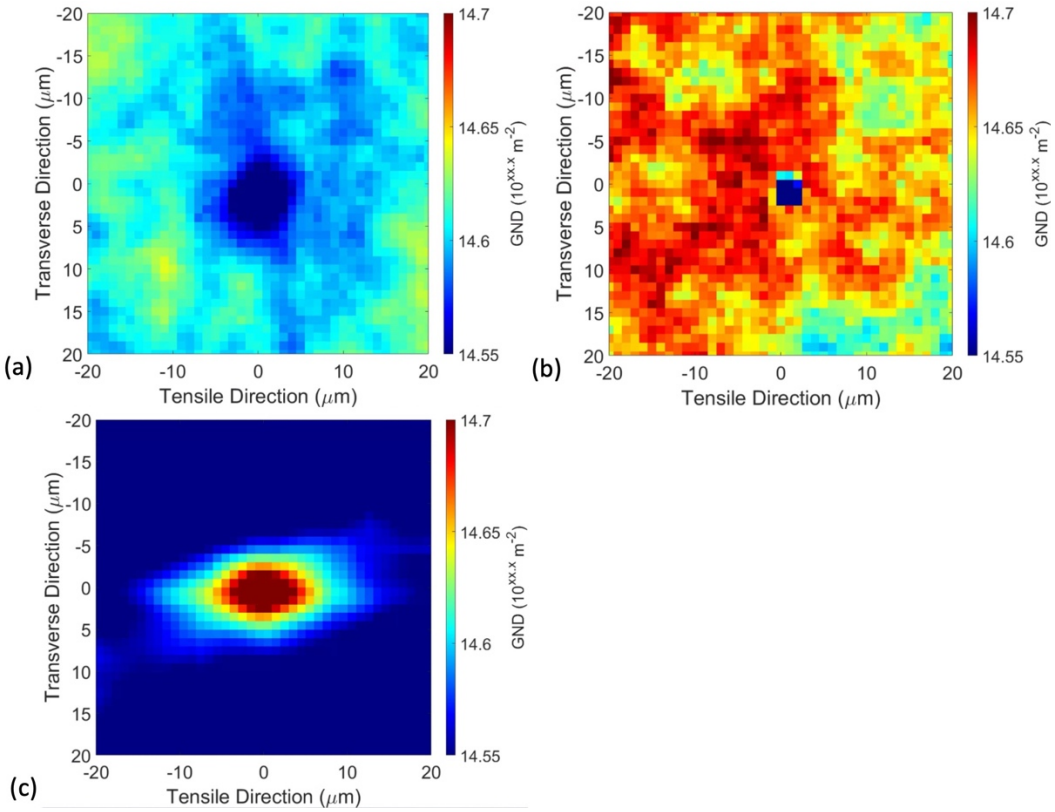


*Figure 9 2-point statistics maps of biaxial-to-uniaxial GNDs vs GBs at ~21.76 µm milled depth (a) and precipitates (b). The same map is shown for simulated GNDs and GBs (c); the simulation does not include precipitates to compare with the measured precipitate statistics. The origin in each map represents the position of GBs or precipitates in each case. Note that the color scale is logarithmic*

GND structures in the vicinity of precipitates, shown in a typical region in Fig. 10, might be explained by the precipitates acting as barriers to dislocation glide, resulting in pileups. Also, as observed by Orowan, incoherency between precipitates and the matrix causes dislocation entanglement which upon further straining nucleates and increases dislocation density [52]. Many examples of GND accumulation at precipitates can be seen, along with shear bands that often pass

through strings of precipitates. These observations are vital for guiding the development of the SG-CPFE model, in order for it to reflect the correct roles of GBs and precipitates in the evolution of GNDs and associated backstress. Currently, the model does not include precipitates; the experimental observation indicates that these will need to be included in order to reflect an important source of strain gradients and internal stress in AA6016-T4.

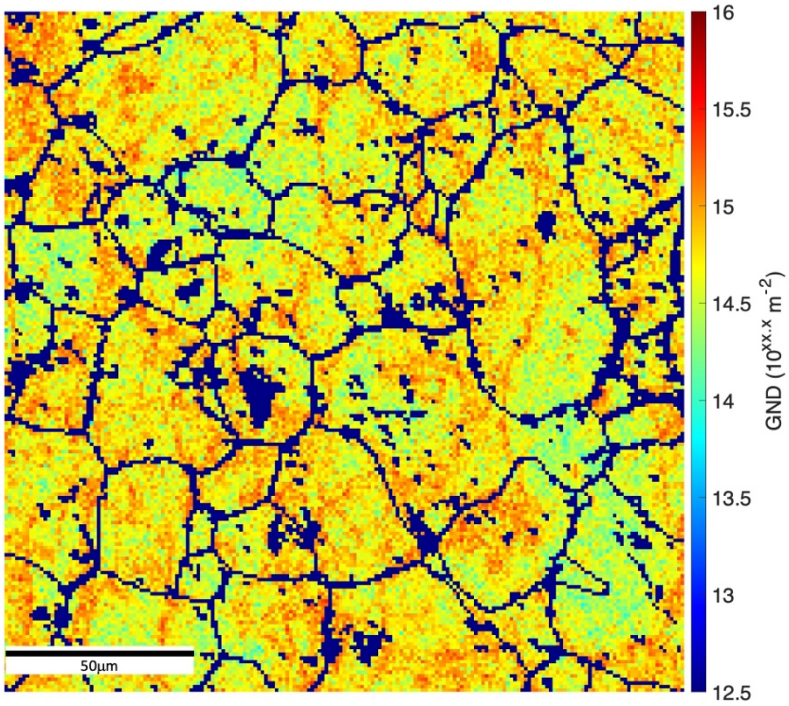


*Figure 10 HREBSD map of the biaxial pre-strained specimen subjected to a subsequent uniaxial tension.*

The direction of slip associated with local strain gradients, and associated GND accumulations, can be visualized by plotting the net Burgers vector (NBV) for both the experimental and simulated GND fields. In the case of the experimental data arising from HREBSD, the Nye tensor encapsulates all information regarding GNDs that is available from the surface measurements taken during an EBSD scan. While there are likely to be many dislocation types present in a given pixel on the EBSD map, the Nye tensor can be thought of as being associated with a single aggregated dislocation, and its related NBV. John Wheeler et al. proposed

that the direction of this Burgers vector could be determined from the right-hand column of the Nye tensor, for which all components are completely defined by the surface measurements taken by HREBSD [53]. This vector was termed the weighted Burgers vector (WBV). More recently, Ruggles et al. suggested a more accurate estimate of the NBV could be achieved by incorporating other measured components of the Nye tensor (rather than simply the third column) [54]. The improved estimate of the NBV, determined for each pixel in the HREBSD map, is the approach taken in the current study.

Figures 11 (a) vs (b) compare the GND and NBV maps at the surface and ~21.76 μm deep into the SVE, correspondingly, for the simulated and experimental samples (left and right, respectively). While full 3D slip information is available for the simulated GND fields, only the same components of the Nye tensor that are available from the experimental data are used to calculate the NBV, in order to make the comparison fair. The simulated maps show that the SG-CPFE model predicts development of strain gradient fields at the grain boundaries, and associated GNDs, while the experimental data indicates higher GND density in the regions of precipitates. The experimental observations of NBVs general alignment in <110> direction within shear bands generally lines up with the predictions from the SG-CPFE model. However, the experimental observation indicates a much wider range of active slip systems, when compared with the simulation (Fig. 11 a). This may be due to precipitates blocking directions with higher Schmid Factors and requiring dislocations to take alternative routes. As mentioned, precipitates are currently not included in the SG-CPFE model. Nevertheless, the model predicts the correct order of magnitude of GNDs.

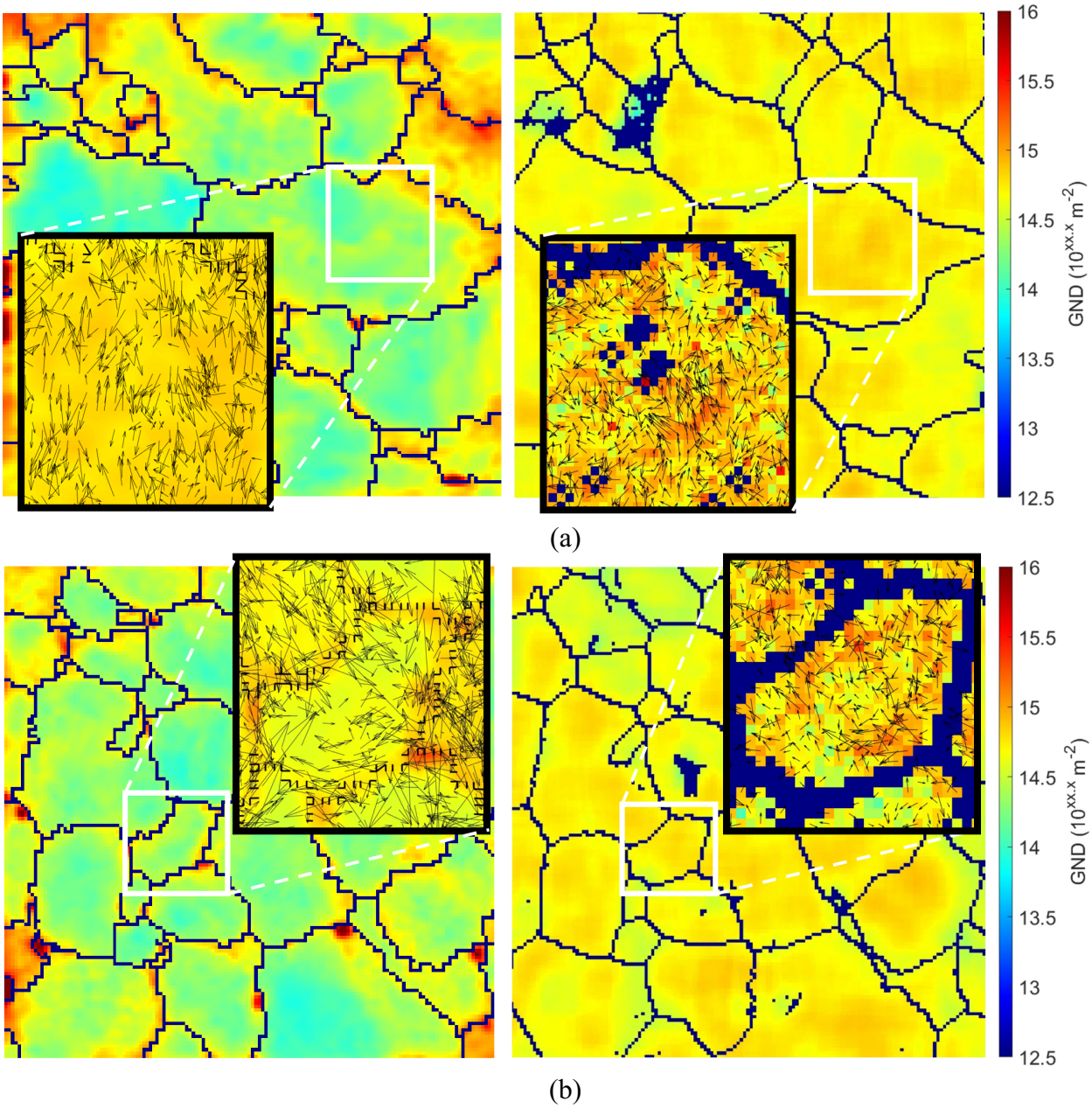


*Figure 11 Comparisons between the WBVs plotted for the experimentally calculated HREBSD-GNDs (right) against the SG-EVPSC mode (left)l calculated GNDs. (a) compares GNDs from the surface layer, and (b) compare GNDs at ~21.76 μm milled depth into biaxial pre-strain specimen with 5.86% subsequent uniaxial strain. The larger images are all 150 μm square. The load is applied in the x-direction (left to right).*

## 5. Conclusions

AA6016-T4 specimens pre-strained under biaxial tension were subsequently deformed under uniaxial tension. A combination of HREBSD, XRD/CMWP, and HRDIC revealed the nature of the formation of GNDs, total DD, and strain gradients across the deformed samples. An SG-CPFE

model was developed for multi-strain path forming, with microstructure reflecting an experimentally collected 3D SVE of a deformed specimen. The following observations were made:

1) Comparison between simulation and experimental data indicates a successful 3D implementation of Gurtin's gradient theory, with slip-level determination of GND content, for strain path changes in AA6016-T4. Calculation of the GND content at the slip level gives effectively equivalent GND evolution as the tradition Nye tensor method, but provides the significant advantage of knowing unambiguously the contribution on each slip system.
2) The model correctly predicts the shape of the dislocation vs strain curve, and also accurately predicts the rapid accumulation of dislocations following a strain path change; it does, however, over-predict the ratio of GND-to-total dislocation densities, potentially due to error in the initial assumed ratio.
3) A detailed 2-point statistics and BSE micrograph analysis revealed that GND development in AA6016-T4 was dominated by precipitates, and GBs did not appear to have an important role in the evolution of strain gradient fields for biaxial tension pre-strained specimens. In the absence of precipitates in the current implementation, the SG-CPFE model predicted that GNDs would mainly accumulate at GBs, highlighting the need for inclusion of precipitates in the model. The net Burgers vector predictions from the model were in general alignment with observed NBVs.
4) Total DD and GND followed a $\varepsilon^{0.6}$ curve with GND trends almost lying flat which was similar for all three pre-strain cases. Therefore, an increase in total DD for later applied strains must be associated with SSD increase which is in agreement with Ashby's theory (Ashby 1970).
5) A strain path change demonstrated a significant increase in dislocation activity in comparison to single strain path deformation for a final 20% effective strain. However,

biaxial-to-uniaxial samples had lower yield stresses and 5% and 2% higher strain-to-failure, respectively, in comparison to uniaxial tension; i.e. the higher dislocation content did not result in lower ductility. The observations indicate the significantly lower level of latent hardening of other slip systems, compared to self-hardening on the active slip systems, during the initial pre-strain. Subsequent strain path change leads to relatively easier slip and lower yield stresses in comparison to uniaxial-to-uniaxial deformation, but rapid accumulation of dislocation density on the newly active systems – for both total and GND densities.

6) Maps of the NBV, indicating the net local direction of slip, showed similar trends for both the experimental and simulated data, with a wide range of scatter in directionality. Qualitative inspection of experimental NBV maps revealed slip to be better aligned in <110> directions in regions of high strain gradient fields, but more random in other areas.

**Acknowledgements**

The work presented in this paper was supported by National Science Foundation grant number CMMI-1926662 (BYU) and CMMI-1926677 (UNH). The authors wish to thank Professor Tamas Ungar for his invaluable help in applying the CMWP technique to the XRD data, and Dr. Stacey Smith at BYU for helping with data collection.

**Declaration of Interests**

The authors declare that they have no known competing financial interests or personal relationships that could have appeared to influence the work reported in this paper.

**References**

[1] S.R. Kalidindi, C.A. Bronkhorst, L. Anand, Crystallographic Texture Evolution in Bulk Deformation Processing of Fcc Metals, Journal of the Mechanics and Physics of Solids 40(3) (1992) 537-569.
[2] F. Roters, P. Eisenlohr, L. Hantcherli, D.D. Tjahjanto, T.R. Bieler, D. Raabe, Overview of constitutive laws, kinematics, homogenization and multiscale methods in crystal plasticity finite-element modeling: Theory, experiments, applications, Acta Materialia 58 (2010) 1152–1211.

[3] J.F. Nye, Some geometrical relations in dislocation solids, Acta Metallurgica 1(2) (1953) 153--162.
[4] E. Kroner, Continuum theory of dislocations and self-stresses, Ergebnisse der Angewandten Mathematik 5 (1958) 1327-1347.
[5] A. Ma, F. Roters, D. Raabe, A dislocation density based constitutive model for crystal plasticity FEM including geometrically necessary dislocations Acta Materialia 54(8) (2006) 2179.
[6] M.E. Gurtin, A gradient theory of single-crystal viscoplasticity that accounts for geometrically necessary dislocations, Journal of the Mechanics and Physics of Solids 50(1) (2002) 5--32.
[7] J.W. Kysar, Y. Saito, M.S. Oztop, D. Lee, W.T. Huh, Experimental lower bounds on geometrically necessary dislocation density, International Journal of Plasticity 26 (2010) 1097-1123.
[8] T.J. Ruggles, D.T. Fullwood, J. Kysar, Resolving geometrically necessary dislocations onto individual slip systems using EBSD-based continuum dislocation microscopy, Int. J. Plasticity 76 (2016) 231-243.
[9] M.E. Gurtin, L. Anand, Thermodynamics applied to gradient theories involving the accumulated plastic strain: the theories of Aifantis and Fleck and Hutchinson and their generalization, J. Mech. Phys. Solids 57(3) (2009) 405-421.
[10] M.F. Ashby, The deformation of plastically non-homogeneous materials, Phil. Mag. 21 (1970) 399-424.
[11] Z. Shen, R. Wagoner, W. Clark, Dislocation pile-up and grain boundary interactions in 304 stainless steel, Scripta Materialia 20 (1986) 921.
[12] A. Harte, M. Atkinson, M. Preuss, J.Q. Da Fonseca, A statistical study of the relationship between plastic strain and lattice misorientation on the surface of a deformed Ni-based superalloy, Acta Materialia 195 (2020) 555-570.
[13] T. Turner, P. Shade, J. Schuren, M. Groeber, The influence of microstructure on surface strain distributions in a nickel micro-tension specimen, Modelling and Simulation in Materials Science and Engineering 21(1) (2012) 015002.
[14] E.O. Hall, The Deformation and Ageing of Mild Steel .3. Discussion of Results, Proceedings of the Physical Society of London Section B 64(381) (1951) 747--753.
[15] N.J. Petch, The Cleavage Strength of Polycrystals, Journal of the Iron and Steel Institute 174(1) (1953) 25--28.
[16] U. Borg, Strain gradient crystal plasticity effects on flow localization, International Journal of Plasticity 23(8) (2007) 1400--1416.
[17] C.F. Dahlberg, J. Faleskog, Strain gradient plasticity analysis of the influence of grain size and distribution on the yield strength in polycrystals, European Journal of Mechanics-A/Solids 44 (2014) 1-16.
[18] V. Smyshlyaev, N. Fleck, The role of strain gradients in the grain size effect for polycrystals, Journal of the Mechanics and Physics of Solids 44(4) (1996) 465-495.
[19] R. Sharma, D. Sargeant, S. Daroju, M. Knezevic, M.P. Miles, D.T. Fullwood, Multi-strain path deformation behavior of AA6016-T4: Experiments and crystal plasticity modeling, International Journal of Solids and Structures 244-245 (2022) 111536.
[20] ARAMIS 3D Digital Image Correlation Strain & 3D Deformation, Trillion Optical Test System, 2011.
[21] J.D. Carroll, B.G. Clark, T.E. Buchheit, B.L. Boyce, C.R. Weinberger, An experimental statistical analysis of stress projection factorsin BCC tantalum, Materials Science and Engineering, A 581 (2013) 108-118.
[22] G. Ribárik, T. Ungár, Characterization of the microstructure in random and textured polycrystals and single crystals by diffraction line profile analysis, Material Science and Engineering A 528(1) (2010) 112-121.
[23] G. Ribárik, B. Jóni, T. Ungár, Global optimum of microstructure parameters in the CMWP line-profile-analysis method by combining Marquardt-Levenberg and Monte-Carlo procedures, Journal of Materials Science and Technology 35 (2019) 1508-1514.

[24] A. Borbely, I. Groma, Variance method for the evaluation of particle size and dislocation density from x-ray Bragg peaks, Appl. Phys. Lett. 79 (2001) 1772-1774.
[25] R.J. Asaro, A. Needleman, Texture development and strain hardening in rate dependent polycrystals, Acta Metallurgica et Materialia 33(6) (1985) 923-953.
[26] J.W. Hutchinson, Bounds and self-consistent estimates for creep of polycrystalline materials, Proceedings of the Royal Society of London. Series A, Mathematical and Physical Sciences (348) (1976) 101-126.
[27] M. Zecevic, I.J. Beyerlein, R.J. McCabe, B.A. McWilliams, M. Knezevic, Transitioning rate sensitivities across multiple length scales: Microstructure-property relationships in the Taylor cylinder impact test on zirconium, Int. J. Plast. 84 (2016) 138-159.
[28] M. Ardeljan, I.J. Beyerlein, M. Knezevic, A dislocation density based crystal plasticity finite element model: Application to a two-phase polycrystalline HCP/BCC composites, J. Mech. Phys. Solids 66(0) (2014) 16-31.
[29] M. Jahedi, M. Ardeljan, I.J. Beyerlein, M.H. Paydar, M. Knezevic, Enhancement of orientation gradients during simple shear deformation by application of simple compression, J. Appl. Phys. 117(21) (2015) 214309.
[30] U.F. Kocks, H. Mecking, Physics and phenomenology of strain hardening: the FCC case, Progress in Materials Science 48(3) (2003) 171-273.
[31] U. Kocks, A. Argon, M. Ashby, Progress in Material Science Vol. 19: Thermodynamics and Kinetics of Slip, Editors: Chalmers B., Christian JW, Massalski TB, Pergamon Press Ltd., Headington Hill Hall, Oxford, England, 1975.
[32] I. Beyerlein, C. Tomé, A dislocation-based constitutive law for pure Zr including temperature effects, International Journal of Plasticity 24(5) (2008) 867-895.
[33] M. Knezevic, D.J. Savage, A high-performance computational framework for fast crystal plasticity simulations, Computational Materials Science 83 (2014) 101-106.
[34] M. Knezevic, R.J. McCabe, C.N. Tomé, R.A. Lebensohn, S.R. Chen, C.M. Cady, G.T. Gray III, B. Mihaila, Modeling mechanical response and texture evolution of α-uranium as a function of strain rate and temperature using polycrystal plasticity, International Journal of Plasticity 43 (2013) 70-84.
[35] R. Madec, B. Devincre, L. Kubin, T. Hoc, D. Rodney, The role of collinear interaction in dislocation-induced hardening, Science 301(5641) (2003) 1879-1882.
[36] A. Eghtesad, M. Knezevic, High-performance full-field crystal plasticity with dislocation-based hardening and slip system back-stress laws: Application to modeling deformation of dual-phase steels, J. Mech. Phys. Solids 134 (2020) 103750.
[37] R. Madec, B. Devincre, L.P. Kubin, From dislocation junctions to forest hardening, Physical review letters 89(25) (2002) 255508.
[38] H. Mecking, U. Kocks, Kinetics of flow and strain-hardening, Acta Metallurgica 29(11) (1981) 1865-1875.
[39] F. Lavrentev, The type of dislocation interaction as the factor determining work hardening, Materials Science and Engineering 46(2) (1980) 191-208.
[40] M. Zecevic, M. Knezevic, Latent hardening within the elasto-plastic self-consistent polycrystal homogenization to enable the prediction of anisotropy of AA6022-T4 sheets, Int. J. Plast. 105 (2018) 141-163.
[41] U. Essmann, and Mughrabi, H., Annihilation of Dislocations During Tensile and Cyclic Deformation and Limits of Dislocation Densities, Philosophical Magazine A 40 (1979) 731-756.
[42] H. Mughrabi, Two-parameter description of heterogeneous dislocation distributions in deformed metal crystals., Materials Science and Engineering 85(1-2) (1987) 15-31.
[43] J.F. Nye, Some geometrical relations in dislocated crystals, Acta Metall. 1(2) (1953) 153-162.

[44] M.E. Gurtin, A gradient theory of single-crystal viscoplasticity that accounts for geometrically necessary dislocations, J. Mech. Phys. Solids 50(1) (2002) 5-32.
[45] S. Daroju, T. Kuwabara, R. Sharma, D.T. Fullwood, M.P. Miles, M. Knezevic, Experimental characterization and crystal plasticity modeling for predicting load reversals in AA6016-T4 and AA7021-T79, International Journal of Plasticity 153 (2022) 103292.
[46] T. Hoc, B. Devincre, L. Kubin, Deformation stage I of FCC crystals: Constitutive modelling, 25 th Riso International Symposium on Materials Science 2004, 2004, pp. 43-59.
[47] B. Devincre, L. Kubin, T. Hoc, Physical analyses of crystal plasticity by DD simulations, Scr. Mater. 54(5) (2006) 741-746.
[48] M.-S. Pham, A. Creuziger, M. Iadicola, A.D. Rollett, Roles of texture and latent hardening on plastic anisotropy of face-centered-cubic materials during multi-axial loading, Journal of the Mechanics and Physics of Solids 99 (2017) 50-69.
[49] L.T. Hansen, J.D. Carroll, E.R. Homer, R.H. Wagoner, G. Zhou, D.T. Fullwood, Character and Distribution of Geometrically Necessary Dislocations in Polycrystalline Tantalum, Microscopy and Microanalysis (2023) ozad049.
[50] T. Ruggles, S. Cluff, M. Miles, D. Fullwood, C. Daniels, A. Avila, M. Chen, Ductility of Advanced High Strength Steel in the Presence of a Sheared Edge, JOM 68(7) (2016) 1839-1849.
[51] R. Sperry, A. Harte, J.Q. da Fonseca, E.R. Homer, R.H. Wagoner, D.T. Fullwood, Slip band characteristics in the presence of grain boundaries in nickel-based superalloy, Acta Materialia 193 (2020) 229-238.
[52] E. Orowan, Mechanical strength properties and real structure of crystals, Zeitschrift Fur Kristallographie 89(3/4) (1934) 327-343.
[53] J. Wheeler, E. Mariani, S. Piazolo, D. Prior, P. Trimby, M. Drury, The weighted Burgers vector: a new quantity for constraining dislocation densities and types using electron backscatter diffraction on 2D sections through crystalline materials, Journal of microscopy 233(3) (2009) 482-494.
[54] T.J. Ruggles, J.I. Deitz, A.A. Allerman, C.B. Carter, J.R. Michael, Identification of star defects in gallium nitride with HREBSD and ECCI, Microscopy and Microanalysis 27(2) (2021) 257-265.